2023 IEEE International Conference on Robotics and Automation (ICRA 2023)
May 29 - June 2, 2023. London, UK

Contact Force Control with Continuously Compliant Robotic Legs

Robin Bendfeld and C. David Remy, *Member, IEEE*

***Abstract*— This paper presents a novel robotic leg design and an associated control approach, which aims at providing an extension to the classical series elastic actuation concept. We propose to directly integrate the series compliance into the structure of the robotic leg itself, as opposed to co-locating spring and motor as done in traditional series elastic actuators. Our approach will eliminate mechanical design complexity and lead to a reduction of mass in the legs. This will, as a secondary benefit, improve the energy efficiency of locomotion. The primary contribution of this work is a model-based controller that can stably and precisely regulate the ground contact forces during stance. This control approach is demonstrated in a set of test-bench experiments, in which we control the contact forces of a modified version of the robotic leg Scarl*ETH*. Here, the rigid shank is replaced by a continuously compliant element made of spring steel. This work presents the first step towards a new generation of robotic legs with structural compliance.**

I. Introduction

In this work, we present a robotic leg design and an associated control concept, which aims at providing an extension of the classical series elastic actuation (SEA) concept [1], [2], [3], [4]. In SEA, an elastic element is inserted between the motors/gears and the driven joint. It is a popular actuator choice in legged robotics, as it enables high fidelity torque control in robots with electrical motors and large gear ratios. For such high-geared motors, frictional effects in the gear box can render traditional torque control impossible. In addition, the gears are protected from impacts, and elastic energy can be stored temporarily in the actuators [5]. Consequently, the concept has found numerous applications in legged robots as well as robotic prostheses [6], [7], [8], [9], [10].

In traditional SEA, each joint contains its own elastic element, often a discrete torsional spring, that is placed between the output of the motor/gearbox and the driven joint (Fig. 1). Without the need for additional force sensors, joint torques can be estimated from measurements of the spring deflection and a known spring characteristic. Regulating this spring deflection then allows for precise control of the joint torques. With the elasticity being located at the individual joints, the rest of the robotic leg is built rigid, which yields a simple kinematic description and allows for modeling the robot as a rigid-body dynamic system.

Despite these advantages, this may not be the most optimal choice from a design perspective. Making the structure rigid, adds mass to a robot's leg, which is even further increased by including the additional elastic element. In addition, the co-location of motor, gearbox, spring, and joint increases the complexity and thus the cost of the design. In this work, we explore an alternative approach, in which the series elasticity is directly integrated into the structure of the robotic leg. In other words, we turn the leg itself into the series elastic element. This greatly simplifies the design and allows for a two-fold reduction in mass. Since the leg segments will become continuously deformable, they can be built slender and lightweight; for example, from carbon-fiber composite structures. Furthermore, no steel springs or other additional elastic elements need to be added to the joints. This reduction in mass is enabled in a location in which it has a disproportional large positive effect on the overall energetics of a legged system [11]. These improvements will hence extend the robots' battery lives and operation range, which are particularly important for robots used in inspection or search and rescue missions.

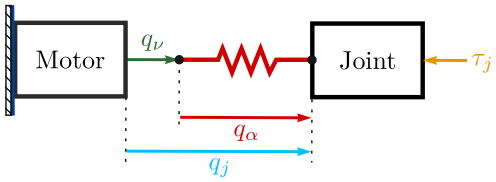

Fig. 1: Schematic of a traditional series elastic actuator located at joint j. The overall joint displacement is given by q_j. It is the sum of motor position q_ν and spring deflection q_α. For a linear elastic element, the joint torque τ_j is given as $\tau_j = -kq_\alpha = k(q_\nu - q_j)$.

The proposed simplified design comes at the cost of an increased complexity for sensing, modeling, simulating, and controlling the forces generated in such a robotic leg. As first step towards overcoming these challenges, this paper presents a model-based control strategy to regulate the ground contact forces of such a robotic leg during the stance phase. To this end, we develop a quasi-static description of the elastic deformation that is used in a velocity-based control approach. This controller is experimentally validated in a test-bench setup with the robotic leg Scarl*ETH*, in which the rigid shank has been replaced with a continuously deformable element.

The design of this continuously compliant shank, is similar to running prostheses in human amputee athletes, which enable these athlete to perform at almost non-amputee level in terms of sprinting and jumping. A similar design has been employed, for example, in the robot RHex, which used six glass-fiber half-circle-shaped legs for maneuvering

*This material is based on work supported by the Vector Stiftung and the Max Planck Research School for Intelligent Systems (IMPRS-IS). We thank Simon R. Eugster for introducing us to the world of continuum mechanics and Simon Sailer for the fruitful discussions.

The authors are with the Institute for Nonlinear Mechanics, Department of Mechanical Engineering, University of Stuttgart, Stuttgart, Germany {bendfeld, remy}@inm.uni-stuttgart.de

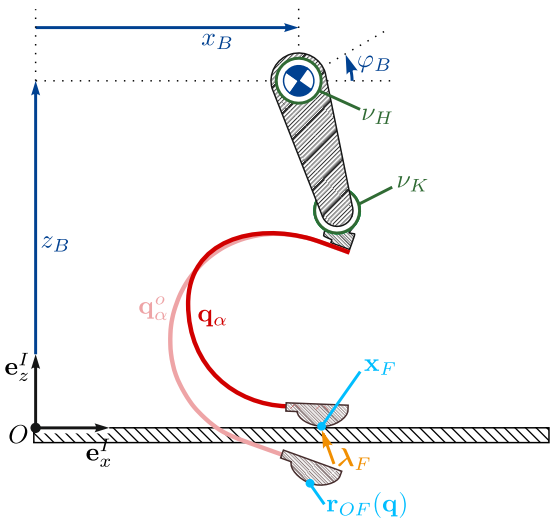

Fig. 2: Model of a robotic leg with continuously compliant shank. The attachment point to the robot's main body is given by $\mathbf{q}_B$, the actuated degrees of freedom are denoted with $\mathbf{q}_\nu$. The curvature of the shank is approximated using $\mathbf{q}_\alpha$, while the corresponding undeformed configuration (shown in light red) is denoted by $\mathbf{q}_\alpha^o$. The forward kinematics of the foot are given by $\mathbf{r}_{OF}(\mathbf{q})$. The contact forces $\boldsymbol{\lambda}_F$ act on a unique contact point on the ground, labeled $\mathbf{x}_F$.

over unstructured terrain [12]. There also exist four legged robots, designed for operation on the moon [13], and a two legged robot for fast running [14] with similar leg designs. In our work, we further extend the idea of designing a robot with such continuously compliant legs towards using this compliance to achieve stable force control.

In the remainder of this paper, we first introduce a suitable model for this robotic leg (Section II) and then develop the necessary theory for control (Section III). Finally, we present the experimental evaluation of this controller in a test bench setup (Section IV) and discuss the results (Section V).

II. Mechanical Model

In the following, we consider the stance phase of a planar robotic leg with a continuously compliant shank (Fig. 2). The kinematics of this leg are described by the generalized coordinate vector

$$\mathbf{q} = \begin{bmatrix}\mathbf{q}_B^{\mathrm{T}} & \mathbf{q}_\nu^{\mathrm{T}} & \mathbf{q}_\alpha^{\mathrm{T}}\end{bmatrix}^{\mathrm{T}}. \tag{1}$$

Here, $\mathbf{q}_B \in \mathbb{R}^{n_B}$ denote the position and orientation of the leg attachment point at the robot's body. In the planar case, $n_B = 3$ and $\mathbf{q}_B = \begin{bmatrix}x_B & z_B & \varphi_B\end{bmatrix}^{\mathrm{T}}$. The actuated degrees of freedom, i.e. the hip and knee joints, are denoted as $\mathbf{q}_\nu = \begin{bmatrix}\nu_H & \nu_K\end{bmatrix} \in \mathbb{R}^{n_\nu}$. Finally, we use a finite approximation $\mathbf{q}_\alpha \in \mathbb{R}^{n_\alpha}$ to represent the deformation of the continuous compliance of the shank. Given the serial arrangement of these degrees of freedom, the location of the foot contact point can be described as a forward kinematic function of the generalized coordinates:

$$\mathbf{r}_{OF} = \mathbf{r}_{OF}(\mathbf{q}). \tag{2}$$

During the stance phase, the equations of motion (EOM) of the leg are described by the differential algebraic equation

$$\begin{aligned}\mathbf{M}(\mathbf{q})\ddot{\mathbf{q}} - \mathbf{f}^{cg}(\mathbf{q},\dot{\mathbf{q}}) &= \boldsymbol{\tau}(\mathbf{q},\dot{\mathbf{q}}) + \mathbf{W}_F(\mathbf{q})\boldsymbol{\lambda}_F \\ \mathbf{g}_F(\mathbf{q},\mathbf{x}_F) &= \mathbf{0},\end{aligned} \tag{3}$$

where $\mathbf{M}$ is the mass matrix and $\mathbf{f}^{cg}$ denote the coriolis, centrifugal and gravitational forces. The vector of generalized forces $\boldsymbol{\tau}$ is specified as

$$\boldsymbol{\tau}(\mathbf{q},\dot{\mathbf{q}}) = \begin{bmatrix}\boldsymbol{\tau}_B^{\mathrm{T}} & \boldsymbol{\tau}_\nu^{\mathrm{T}} & \boldsymbol{\tau}_\alpha^{\mathrm{T}}(\mathbf{q},\dot{\mathbf{q}}),\end{bmatrix}^{\mathrm{T}} \tag{4}$$

with the generalized reaction forces and moments at the attachment point to the body $\boldsymbol{\tau}_B$, the actuator torques $\boldsymbol{\tau}_\nu$ and the generalized elastic torques $\boldsymbol{\tau}_\alpha$. Ground contact is modelled by the bilateral constraint $\mathbf{g}_F$:

$$\mathbf{g}_F(\mathbf{q},\mathbf{x}_F) = \mathbf{r}_{OF}(\mathbf{q}) - \mathbf{x}_F = \mathbf{0}, \tag{5}$$

where $\mathbf{x}_F$ denotes the position of the contact point on the ground. This position is determined at the beginning of the stance phase and, since we assume no sliding, remains fixed. That is, $\dot{\mathbf{x}}_F = \mathbf{0}$ and thus $\mathbf{W}_F^T\dot{\mathbf{q}} = \dot{\mathbf{r}}_{OF}(\mathbf{q}) = \mathbf{0}$, with the associated constraint Jacobian:

$$\mathbf{W}_F^T(\mathbf{q}) = \frac{\partial \mathbf{g}_F}{\partial \mathbf{q}} = \begin{bmatrix}\mathbf{W}_B^{\mathrm{T}} & \mathbf{W}_\nu^{\mathrm{T}} & \mathbf{W}_\alpha^{\mathrm{T}}\end{bmatrix}. \tag{6}$$

The corresponding contact forces are $\boldsymbol{\lambda}_F = \begin{bmatrix}\lambda_x & \lambda_z\end{bmatrix}^{\mathrm{T}}$.

To model the continuously compliant shank, we use a discrete approximation in the form of an inextensible Hencky-type beam (Fig. 3) [15]. With this formulation, the potential elastic energy is given as:

$$V^k(\mathbf{q}_\alpha,\mathbf{q}_\alpha^o) = \frac{1}{2}\left(\mathbf{q}_\alpha - \mathbf{q}_\alpha^o\right)^{\mathrm{T}}\mathbf{K}\left(\mathbf{q}_\alpha - \mathbf{q}_\alpha^o\right), \tag{7}$$

with the stiffness matrix $\mathbf{K} = c\mathbf{I}_{n_\alpha \times n_\alpha}$[16]. Here, the discretized bending stiffness is calculated as $c = \frac{EI}{L}n_\alpha$ with the Young's modulus E, the second moment of area I and the total length of the continuum L. The reference configuration of the undeformed shank is described by $\mathbf{q}_\alpha^o$ [17], [18]. The generalized visco-elastic torques acting in the continuously compliant element are given as $\boldsymbol{\tau}_\alpha(\mathbf{q},\dot{\mathbf{q}}) = \mathbf{f}^k(\mathbf{q}_\alpha) + \mathbf{f}^d(\dot{\mathbf{q}}_\alpha)$ with the elastic force

$$\mathbf{f}^k(\mathbf{q}_\alpha) = -\left(\frac{\partial V^k}{\partial \mathbf{q}_\alpha}\right)^{\mathrm{T}}(\mathbf{q}_\alpha,\mathbf{q}_\alpha^o) = -\mathbf{K}(\mathbf{q}_\alpha - \mathbf{q}_\alpha^o) \tag{8}$$

and the damping force $\mathbf{f}^d(\dot{\mathbf{q}}_\alpha)$.

III. Controller Development

For the system described in (1)-(8) we derive a control law to regulate the contact forces $\boldsymbol{\lambda}_F$ between the foot and the ground at point $\mathbf{x}_F$. To this end, we interpret the entire leg as an extension to a classical series elastic actuator, as described in [1], [2], [4]. That is, we use the motor velocities to regulate the deflection of the compliant shank and, in turn, control the contact forces. This is facilitated by a number of simplifying assumptions.

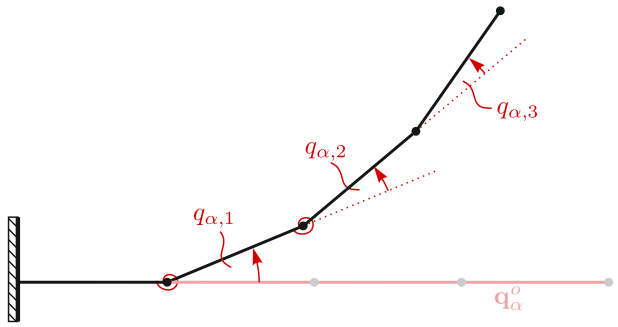

Fig. 3: Discrete approximation of the continuously compliant shank using an inextensible formulation of the Hencky-type beam theory. The deformation is described by the vector $\mathbf{q}_\alpha$ and the reference configuration of the undeformed shank is given by $\mathbf{q}_\alpha^o$. The red circles show the location of some of the torsional springs.

A. Controller Preliminaries

1) Reducing the EOM to a quasi-static equilibrium: As primary simplification, we neglect inertial, gravitational, and damping forces. During stance, when the leg is loaded, these effects are much smaller than the forces created by the elastic deformation; — particularly for the light-weight robotic leg we consider in our work. As a result of this simplification, eq. (3) reduces to the quasi-static equilibrium

$$\mathbf{0} = \begin{bmatrix} \boldsymbol{\tau} + \mathbf{W}_F(\mathbf{q})\boldsymbol{\lambda}_F \\ \mathbf{g}_F(\mathbf{q}, \mathbf{x}_F) \end{bmatrix} = \begin{bmatrix} \boldsymbol{\tau}_B + \mathbf{W}_B(\mathbf{q})\boldsymbol{\lambda}_F \\ \boldsymbol{\tau}_\nu + \mathbf{W}_\nu(\mathbf{q})\boldsymbol{\lambda}_F \\ \mathbf{f}^k(\mathbf{q}) + \mathbf{W}_\alpha(\mathbf{q})\boldsymbol{\lambda}_F \\ \mathbf{r}_{OF}(\mathbf{q}) - \mathbf{x}_F \end{bmatrix}. \tag{9}$$

Since inertial effects are removed, the individual equations from eq. (9) are only coupled on configuration level. Assuming that we are able to measure the position of the main body and the actuated joints, we can consider the two bottom rows individually, and define a residual $\mathbf{r}$ that implicitly couples the configuration with the contact position and contact forces:

$$\mathbf{r}(\mathbf{q}, \mathbf{x}_F, \boldsymbol{\lambda}_F) = \begin{bmatrix} -\mathbf{K}(\mathbf{q}_\alpha - \mathbf{q}_\alpha^o) + \mathbf{W}_\alpha(\mathbf{q})\boldsymbol{\lambda}_F \\ \mathbf{r}_{OF}(\mathbf{q}) - \mathbf{x}_F \end{bmatrix} = \mathbf{0}. \tag{10}$$

Using the implicit function theorem [19], we convert this implicit expression into an explicit input-output relationship. Here, we define the generalized coordinates describing the deformation of the shank $\mathbf{q}_\alpha$ and the contact forces $\boldsymbol{\lambda}_F$ as the outputs, while the inputs are the positions of the actuated joints $\mathbf{q}_\nu$, the position and orientation of the body attachment point $\mathbf{q}_B$ as well as the position of the foot contact point $\mathbf{x}_F$. For variations in the inputs and the outputs, this explicit relationship is given by:

$$\begin{bmatrix} \mathrm{d}\mathbf{q}_\alpha \\ \mathrm{d}\boldsymbol{\lambda}_F \end{bmatrix} = -\left(\frac{\partial \mathbf{r}}{\partial \begin{bmatrix} \mathbf{q}_\alpha^\mathrm{T} & \boldsymbol{\lambda}_F^\mathrm{T} \end{bmatrix}} \right)^{-1} \frac{\partial \mathbf{r}}{\partial \begin{bmatrix} \mathbf{q}_\nu^\mathrm{T} & \mathbf{q}_B^\mathrm{T} & \mathbf{x}_F^\mathrm{T} \end{bmatrix}} \begin{bmatrix} \mathrm{d}\mathbf{q}_\nu \\ \mathrm{d}\mathbf{q}_B \\ \mathrm{d}\mathbf{x}_F \end{bmatrix}, \tag{11}$$

with

$$\frac{\partial \mathbf{r}}{\partial \begin{bmatrix} \mathbf{q}_\alpha^\mathrm{T} & \boldsymbol{\lambda}_F^\mathrm{T} \end{bmatrix}} = \begin{bmatrix} \mathbf{K}_{\alpha\lambda} & \mathbf{W}_\alpha \\ \mathbf{W}_\alpha^\mathrm{T} & \mathbf{0} \end{bmatrix} \tag{12}$$

and

$$\frac{\partial \mathbf{r}}{\partial \begin{bmatrix} \mathbf{q}_\nu^\mathrm{T} & \mathbf{q}_B^\mathrm{T} & \mathbf{x}_F^\mathrm{T} \end{bmatrix}} = \begin{bmatrix} \frac{\partial \mathbf{W}_\alpha \boldsymbol{\lambda}_F}{\partial \mathbf{q}_\nu} & \frac{\partial \mathbf{W}_\alpha \boldsymbol{\lambda}_F}{\partial \mathbf{q}_B} & \mathbf{0} \\ \mathbf{W}_\nu^\mathrm{T} & \mathbf{W}_B^\mathrm{T} & -\mathbf{I} \end{bmatrix}. \tag{13}$$

Here, $\mathbf{K}_{\alpha\lambda}(\mathbf{q}, \boldsymbol{\lambda}_F) = \frac{\partial \mathbf{f}^k}{\partial \mathbf{q}_\alpha} + \frac{\partial \mathbf{W}_\alpha \boldsymbol{\lambda}}{\partial \mathbf{q}_\alpha}$ represents the effective stiffness matrix.

Equation (10) can only be locally inverted if the matrix in eq. (12) is non-singular. To this end, we first analyze whether $\mathbf{K}_{\alpha\lambda}$ is invertible. This is the case, as long as the static equilibrium in eq. (10) is a local minimum of the associated potential energy or, in other words, if the static equilibrium is stable [20]. If $\mathbf{K}_{\alpha\lambda}$ is invertible, we can compute

$$\mathbf{G}_K(\mathbf{q}, \boldsymbol{\lambda}_F) \coloneqq \mathbf{0} - \mathbf{W}_\alpha^\mathrm{T} \mathbf{K}_{\alpha\lambda}^{-1} \mathbf{W}_\alpha. \tag{14}$$

The matrix $\mathbf{G}_K$ is invertible as long as the contact constraints are linearly independent; that is, as long as the compliant shank is not in a singular configuration. Under this condition of a non-singular, stable equilibrium, we use the Schur complement to express the inverse of the matrix in (12):

$$\left(\frac{\partial \mathbf{r}}{\partial \begin{bmatrix} \mathbf{q}_\alpha^\mathrm{T} & \boldsymbol{\lambda}_F^\mathrm{T} \end{bmatrix}} \right)^{-1} = \begin{bmatrix} \mathbf{r}_{\alpha\alpha} & \mathbf{r}_{\alpha\lambda} \\ \mathbf{r}_{\alpha\lambda}^\mathrm{T} & \mathbf{r}_{\lambda\lambda} \end{bmatrix}, \tag{15}$$

where the entries of the inverse matrix read as

$$\mathbf{r}_{\alpha\alpha}(\mathbf{q}, \boldsymbol{\lambda}_F) = \mathbf{K}_{\alpha\lambda}^{-1} + \mathbf{K}_{\alpha\lambda}^{-1} \mathbf{W}_\alpha \mathbf{G}_K^{-1} \mathbf{W}_\alpha^\mathrm{T} \mathbf{K}_{\alpha\lambda}^{-1} \tag{16}$$

$$\mathbf{r}_{\alpha\lambda}(\mathbf{q}, \boldsymbol{\lambda}_F) = -\mathbf{K}_{\alpha\lambda}^{-1} \mathbf{W}_\alpha \mathbf{G}_K^{-1} \tag{17}$$

$$\mathbf{r}_{\lambda\lambda}(\mathbf{q}, \boldsymbol{\lambda}_F) = \mathbf{G}_K^{-1}. \tag{18}$$

Using these results, we rewrite the differential relationship:

$$\begin{aligned} \begin{bmatrix} \mathrm{d}\mathbf{q}_\alpha \\ \mathrm{d}\boldsymbol{\lambda}_F \end{bmatrix} = &- \begin{bmatrix} \mathbf{r}_{\alpha\alpha} & \mathbf{r}_{\alpha\lambda} \\ \mathbf{r}_{\alpha\lambda}^\mathrm{T} & \mathbf{r}_{\lambda\lambda} \end{bmatrix} \begin{bmatrix} \frac{\partial \mathbf{W}_\alpha \boldsymbol{\lambda}_F}{\partial \mathbf{q}_\nu} \\ \mathbf{W}_\nu^\mathrm{T} \end{bmatrix} \mathrm{d}\mathbf{q}_\nu \\ &- \begin{bmatrix} \mathbf{r}_{\alpha\alpha} & \mathbf{r}_{\alpha\lambda} \\ \mathbf{r}_{\alpha\lambda}^\mathrm{T} & \mathbf{r}_{\lambda\lambda} \end{bmatrix} \begin{bmatrix} \frac{\partial \mathbf{W}_\alpha \boldsymbol{\lambda}_F}{\partial \mathbf{q}_B} \\ \mathbf{W}_B^\mathrm{T} \end{bmatrix} \mathrm{d}\mathbf{q}_B \\ &- \begin{bmatrix} \mathbf{r}_{\alpha\alpha} & \mathbf{r}_{\alpha\lambda} \\ \mathbf{r}_{\alpha\lambda}^\mathrm{T} & \mathbf{r}_{\lambda\lambda} \end{bmatrix} \begin{bmatrix} \mathbf{0} \\ -\mathbf{I} \end{bmatrix} \mathrm{d}\mathbf{x}_F \end{aligned} \tag{19}$$

2) Using actuator velocities as inputs: It is an established approach in traditional SEA to consider the motors as velocity sources rather than torque sources [2]. This is, because most series elastic actuators use highly geared drives, which are not back-drivable, and exhibit a large amount of friction. This makes using the actuator torques $\boldsymbol{\tau}_\nu$ impractical. To facilitate the application of this approach, we interpret the relationship in eq. (19) in terms of velocities, yielding the drift-free differential equation

$$\begin{aligned} \dot{\boldsymbol{x}} &= \begin{bmatrix} \boldsymbol{g}_\alpha \\ \boldsymbol{g}_\lambda \end{bmatrix} \boldsymbol{u} + \begin{bmatrix} \boldsymbol{w}_{\alpha B} \\ \boldsymbol{w}_{\lambda B} \end{bmatrix} \boldsymbol{d} \\ \boldsymbol{\lambda}_F &= \boldsymbol{h}(\boldsymbol{x}) = \begin{bmatrix} \mathbf{0}_{n_F \times n_\alpha} & \mathbf{I}_{n_F \times n_F} \end{bmatrix} \boldsymbol{x}. \end{aligned} \tag{20}$$

Here, the state vector of the system is given as $\boldsymbol{x} = \begin{bmatrix} \mathbf{q}_\alpha^\mathrm{T} & \boldsymbol{\lambda}_F^\mathrm{T} \end{bmatrix}^\mathrm{T}$ and the inputs are the commanded motor velocities: $\boldsymbol{u} = \dot{\mathbf{q}}_\nu$. The velocity of the body is considered to be a disturbance $\boldsymbol{d} = \dot{\mathbf{q}}_B$, while we assume that the foot remains stationary with $\dot{\mathbf{x}}_F = \mathbf{0}$. As stated earlier, the body coordinates $\mathbf{q}_B$ and actuator positions $\mathbf{q}_\nu$ as well as their respective velocities can be measured, such that $\mathbf{q}$ is fully

known. Finally, we included the contact forces $\boldsymbol{\lambda}_F = \boldsymbol{h}(\boldsymbol{x})$ as the (measured) output. The remaining terms are given as:

$$\boldsymbol{g}_\alpha(\mathbf{q}, \boldsymbol{\lambda}_F) = -\begin{bmatrix}\mathbf{r}_{\alpha\alpha} & \mathbf{r}_{\alpha\lambda}\end{bmatrix}\begin{bmatrix}\frac{\partial \mathbf{W}_\alpha \boldsymbol{\lambda}_F}{\partial \mathbf{q}_\nu} \\ \mathbf{W}_\nu^{\mathrm{T}}\end{bmatrix} \tag{21}$$

$$\boldsymbol{g}_\lambda(\mathbf{q}, \boldsymbol{\lambda}_F) = -\begin{bmatrix}\mathbf{r}_{\alpha\lambda}^{\mathrm{T}} & \mathbf{r}_{\lambda\lambda}\end{bmatrix}\begin{bmatrix}\frac{\partial \mathbf{W}_\alpha \boldsymbol{\lambda}_F}{\partial \mathbf{q}_\nu} \\ \mathbf{W}_\nu^{\mathrm{T}}\end{bmatrix} \tag{22}$$

$$= -\mathbf{G}_K^{-1}\left(\mathbf{W}_\nu^{\mathrm{T}} - \mathbf{W}_\alpha^{\mathrm{T}}\mathbf{K}_{\alpha\lambda}^{-1}\frac{\partial \mathbf{W}_\alpha \boldsymbol{\lambda}_F}{\partial \mathbf{q}_\nu}\right) \tag{23}$$

$$\boldsymbol{w}_{\alpha B}(\mathbf{q}, \boldsymbol{\lambda}_F) = -\begin{bmatrix}\mathbf{r}_{\alpha\alpha} & \mathbf{r}_{\alpha\lambda}\end{bmatrix}\begin{bmatrix}\frac{\partial \mathbf{W}_\alpha \boldsymbol{\lambda}_F}{\partial \mathbf{q}_B} \\ \mathbf{W}_B^{\mathrm{T}}\end{bmatrix} \tag{24}$$

$$\boldsymbol{w}_{\lambda B}(\mathbf{q}, \boldsymbol{\lambda}_F) = -\begin{bmatrix}\mathbf{r}_{\alpha\lambda}^{\mathrm{T}} & \mathbf{r}_{\lambda\lambda}\end{bmatrix}\begin{bmatrix}\frac{\partial \mathbf{W}_\alpha \boldsymbol{\lambda}_F}{\partial \mathbf{q}_B} \\ \mathbf{W}_B^{\mathrm{T}}\end{bmatrix} \tag{25}$$

B. Force controller

Our control goal is to track a desired contact force $\boldsymbol{\lambda}_F^d$. That is, $\lim_{t\to\infty} \boldsymbol{\lambda}_F(t) - \boldsymbol{\lambda}_F^d(t) = \mathbf{0}$. Without external disturbances (i.e., $\boldsymbol{d} \equiv \mathbf{0}$), stable error dynamics are achieved by using a P-controller in combination with a feed-forward input

$$\left(\dot{\boldsymbol{\lambda}}_F - \dot{\boldsymbol{\lambda}}_F^d\right) + \boldsymbol{P}_{\boldsymbol{\lambda}}\left(\boldsymbol{\lambda}_F - \boldsymbol{\lambda}_F^d\right) = \mathbf{0}\,, \tag{26}$$

with a positive definite controller matrix $\boldsymbol{P}_{\boldsymbol{\lambda}}$. With the tools from nonlinear control systems (as discussed for example in [21]), we determine the Lie derivatives of the input-output-relation:

$$L_{\boldsymbol{g}}\boldsymbol{h} = \frac{\partial \boldsymbol{h}}{\partial \boldsymbol{x}}\boldsymbol{g} = \begin{bmatrix}\mathbf{0}_{n_F \times n_\alpha} & \mathbf{I}_{n_F \times n_F}\end{bmatrix}\begin{bmatrix}\boldsymbol{g}_\alpha \\ \boldsymbol{g}_\lambda\end{bmatrix} \tag{27}$$

$$= \boldsymbol{g}_\lambda(\mathbf{q}, \boldsymbol{\lambda}_F) \tag{28}$$

For $\mathrm{rank}(\boldsymbol{g}_\lambda) = n_F$ we get a local vector relative degree of $\boldsymbol{r}_u = \mathbf{1}_{n_\nu}$. Thus, we can find a controller for the output of the differential equation by using the expression:

$$\boldsymbol{u} = \boldsymbol{g}_\lambda^{-1}\left(\dot{\boldsymbol{\lambda}}_F^d + \boldsymbol{P}_{\boldsymbol{\lambda}}\left(\boldsymbol{\lambda}_F^d - \boldsymbol{\lambda}_F\right)\right). \tag{29}$$

This control law is applicable, if the inverse of eq. (23) exists. It thus has to hold that:

$$\det\left(\mathbf{W}_\nu^{\mathrm{T}} - \mathbf{W}_\alpha^{\mathrm{T}}\mathbf{K}_{\alpha\lambda}^{-1}\frac{\partial \mathbf{W}_\alpha \boldsymbol{\lambda}_F}{\partial \mathbf{q}_\nu}\right) \neq 0\,. \tag{30}$$

The condition in eq. (30) can be checked offline for a combination of coordinates $\mathbf{q}_\nu$, $\mathbf{q}_B$ and a foot position $\mathbf{x}_F$ by solving the static equilibrium eq. (10) and inserting the resulting $\mathbf{q}_\alpha$ and $\boldsymbol{\lambda}_F$ into eq. (30). Such an evaluation is shown in Fig. 4, where the turquoise line denotes combinations of $\mathbf{q}$, $\boldsymbol{\lambda}_F$ and $\mathbf{x}_F$ for which $\boldsymbol{g}_\lambda$ is not invertible. From a robotics point of view, these values correspond to kinematically singular configurations in which the two motors and the contact point form a straight line. Note, that we fixed the boundaries of horizontal forces in Fig. 4a) to be $\lambda_x \in \{-134, 134\}$N and the vertical force in Fig. 4b) to be $\lambda_z \in \{0, 134\}$N. While negative values of the vertical force can occur when solving the root finding problem of eq. (10), the robotic leg would lift off the ground in those scenarios. We also found, that all the static equilibria shown in Fig. 4 correspond to local minima of the potential energy

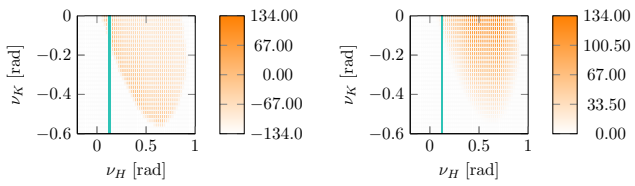

a) λ_x b) λ_z

Fig. 4: The components of the contact forces $\boldsymbol{\lambda}_F$ are computed and shown for a set of body positions $\mathbf{q}_B = \begin{bmatrix}-0.068\mathrm{m} & 0.598\mathrm{m} & 0\mathrm{rad}\end{bmatrix}^{\mathrm{T}}$, hip angle ν_H and knee angle ν_K and foot contact point $\mathbf{x}_F = \mathbf{0}m$. The turquoise line denotes those combinations of $\mathbf{q}$, $\mathbf{x}_F$ and $\boldsymbol{\lambda}_F$ for which $\boldsymbol{g}_\lambda$ is not invertible.

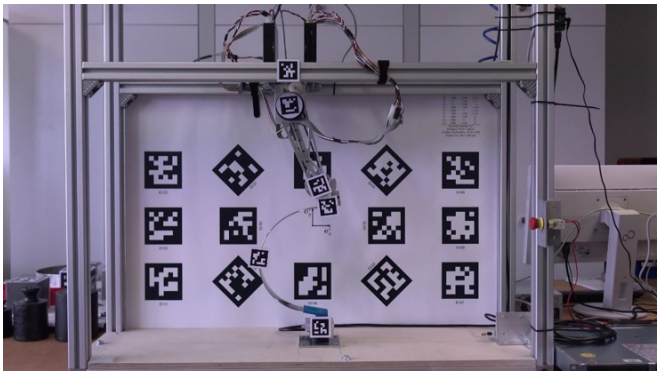

Fig. 5: Testbench setup with a modified version of the robotic leg Starl*ETH* that was used in the experimental evaluation of the controller.

minimization problem. Therefore, they are stable equilibria for the dynamics of the robotic leg [20].

We can extend the control law from eq. (29) for cases in which disturbances are present, for example when the robotic leg is attached to a moving robot. To this end, we compute the relative degree of eq. (20) w.r.t the body velocity:

$$L_{\boldsymbol{w}_B}\boldsymbol{h} = \frac{\partial \boldsymbol{h}}{\partial \boldsymbol{x}}\boldsymbol{w}_B = \boldsymbol{w}_{\lambda B}(\mathbf{q}, \boldsymbol{\lambda}_F). \tag{31}$$

This relative degree $\boldsymbol{r}_d = \mathbf{1}_{n_B}$ and disturbance decoupling is possible. In the special case where the disturbances can be measured, the control law from eq. (29) can be extended to our final controller equation

$$\boldsymbol{u} = \boldsymbol{g}_\lambda^{-1}\left(\dot{\boldsymbol{\lambda}}_F^d + \boldsymbol{P}_{\boldsymbol{\lambda}}\left(\boldsymbol{\lambda}_F^d - \boldsymbol{\lambda}_F\right)\right) - \boldsymbol{g}_\lambda^{-1}\boldsymbol{w}_{\lambda B}\boldsymbol{d}\,. \tag{32}$$

IV. Experiments

For the experimental evaluation of the force controller presented in Section III, we used a modified version (Fig. 5) of the robotic leg Scarl*ETH* which we previously used in the robots RAM*one* and RAM*bi* [4], [22], [23], [24], [25]. The series elastic springs in the hip and knee actuation were disabled and the rigid shank was replaced by a single pre-deformed half-circle shaped continuous compliant component which was manufactured from spring steel.

The controller was implemented on an xPC-target using MATLAB/Simulink Real-Time and EtherCAT as communication protocol. The control loop had a sampling frequency of 1 kHz. The motors used were maxon motors, combined with the maxon EPOS3 motor controllers. The velocity

control loop of those motor controllers runs at 1 kHz, while their internal current control loop has a sampling frequency of 10 kHz. The maxon motors output in our experiment were connected to a harmonic drive with a gear ratio of 50:1. Throughout the experiments, we used a constant force control gain of $\mathbf{P}_\lambda = 10\mathbf{I}_{n_F \times n_F}$.

For all the experiments, the body attachment point was kept fixed at a given position. We used optical encoders in the hip and knee motor to measure joint angles. Furthermore, the test bench was equipped with a wire encoder from SICK and a Rokubi 6-axis F-/T-sensor from BOTA Systems AG to measure the horizontal position of the foot contact point as well as the forces acting between the robots foot contact point and the ground of the test bench, respectively. Force values were measured at 1 kHz and low-pass filtered with a moving-average finite impulse response with a cutoff frequency of 20 Hz. The optical markers visible in Fig. 5 were not used for the experiments. Instead, information about the positions of the body attachment point $\mathbf{q}_B$, the foot contact point $\mathbf{x}_F$ and the hip and knee angles $\mathbf{q}_\nu$ were used to solve eq. (10) at 100 Hz to get an estimate of the deformation states $\mathbf{q}_\alpha$.

In a first experiment, we evaluated the step response of the closed loop system in different settings. Starting with a fixed horizontal force of $\lambda_x^d = 0\,\text{N}$, step changes in the vertical force reference trajectory λ_z^d were applied. In Fig. 6 the successful tracking of the reference contact forces is shown. Our controller was able to stably track the desired reference values with a RMS value of $\lambda_x^{RMS} = 0.085\,\text{N}$, which is within the noise of the F/T-sensor. No significant steady-state error was observed in both force directions. To highlight the dynamic performance, a close-up to the step response is shown in Fig. 7. The rise time of the controller to achieve 90% of the reference step is $t_{rise} = 290\,\text{ms}$. The primary dynamic limitation is the bandwidth of the motors, which require around 80 ms to accelerate to their maximal speed (Fig. 8). We observed a moderate coupling between the two contact forces of 12% in horizontal force direction, when a vertical step is applied. This coupling was more pronounced when we keep the vertical reference force fixed, and applied step inputs to the horizontal contact forces (Fig. 10). Finally, Fig. 9. visualizes the motion of the leg, when subject to steps in both reference contact forces. This is best seen, when looking at the optical marker placed on the actuator.

In a second experiment, we applied a frequency sweep in the vertical force direction

$$\lambda_z^d(t) = a_{\lambda_z} \sin\left(2\pi f_{\lambda_z}(t)t + \phi_{\lambda_z}\right) + b_{\lambda_z}, \qquad (33)$$

with the parameters $a_{\lambda_z} \in \{1,\ 2\}\,\text{N}$, $b_{\lambda_z} \in \{5,\ 10,\ 15\}\,\text{N}$, $\phi_{\lambda_z} = 0\,\text{rad}$ and $f_{\lambda_z}(t) \in \{0.2,\ 0.4,\ 0.6,\ \ldots,\ 10\}\,\text{Hz}$. The estimated transfer function of the closed-loop system is shown in Fig. 11. We observed a resonance frequency of $f_z^{res} \approx 3.9\,\text{Hz}$ and a bandwidth of $f_z^{bw} \approx 8.5\,\text{Hz}$, which is within the range of Pratt's electrical SEAs [3].

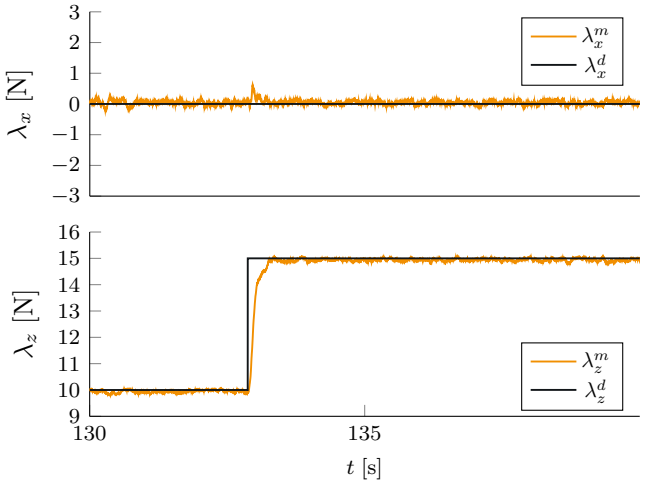

Fig. 6: Desired, shown in black, and measured, orange forces at the foot contact point for step inputs in the vertical force direction.

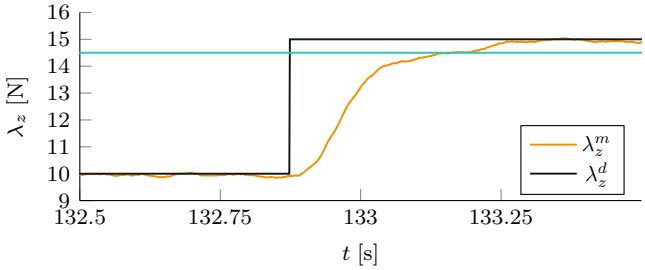

Fig. 7: Close-up of the tracking behavior of the force controller with desired, black and measured, orange vertical contact force. The turquoise line shows the 90% bound for the reference step.

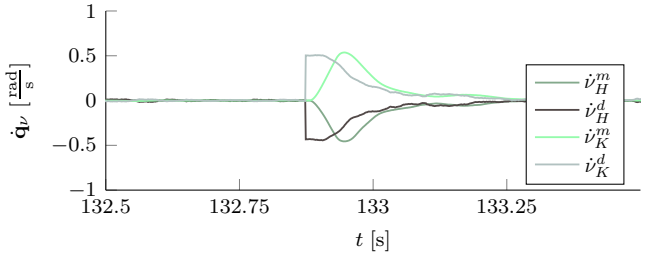

Fig. 8: Close-up of the tracking behavior of the velocity controller of the EPOS with desired hip velocity in black, the measured and filtered hip velocity (olive), the desired (gray) knee and measured and filtered knee (light green) velocities.

V. Conclusion

In this work, we presented a generalization of the traditional series-elastic-actuation concept by integrating the compliance directly into the structure of a robotic leg. Furthermore, we designed and analyzed a quasi-static force controller, which deforms the spring to generate desired forces at the foot contact point. We believe, that the direct integration of compliance within the structure of the robot not only allows for new designs of legged robots, but can also be beneficial in terms of efficiency. This design lead to a higher computational burden, which was tackled successfully by thoroughly modeling the mechanical system and careful parameterization of the controller.

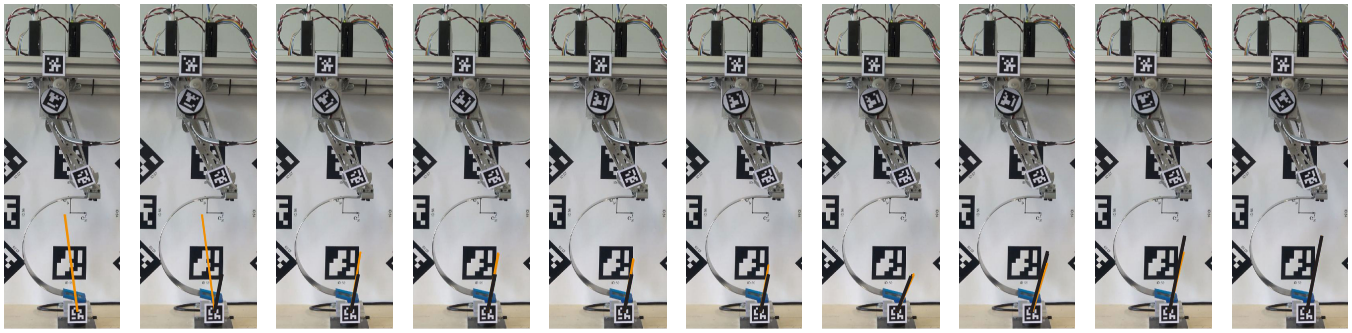

Fig. 9: Snapshots of an experiment with steps on both force reference signals at different times. Desired force vector is given in (-) and measured force vector in (-). In the first picture no reference is given which is shown by the absence of a black line. Pictures (2)-(6) show the convergence of the measured to the desired force value. In the pictures (7)-(10) the change of the reference trajectory and the resulting tracking behavior is shown.

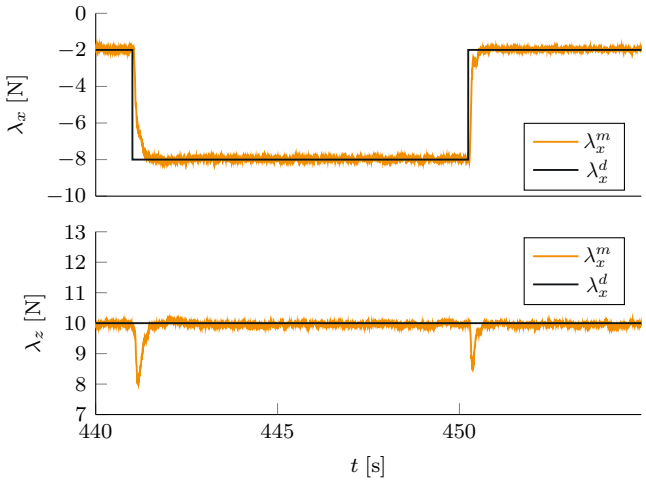

Fig. 10: Desired (black) and measured (orange) forces at the foot contact point for step inputs in the horizontal force direction.

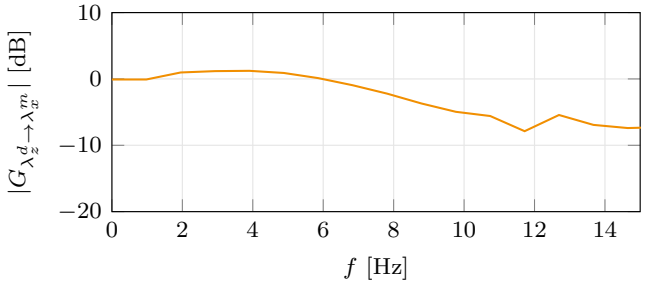

Fig. 11: Estimated closed loop transfer function from the sinusoidal reference trajectory in vertical contat force direction of the MIMO-system.

The primary limitation of our work is that, in the current setup, the forces at the foot contact point are measured by an external force sensor. Without substantial changes to the algorithm, the force sensor could be integrated into the leg at the proximal connection of the elastic shank. As a drawback of this approach, the associated mass and cost might counteract the intended benefit of our design. As an alternative, strain gauges in combination with a suitable state estimator could be used to obtain similar force data at highly reduced mass, but at the cost of higher computational complexity. Furthermore, the elasticity can create unwanted deformations during swing, which requires a suitable controller for swing foot placement. Similar to the approach described in [4], nonlinear damping can facilitated this task.

In this very simple modification of the existing Scarl*ETH*design and with an elastic element made from heavy spring steel, we already saw a reduction in the mass of the robotic shank. It is likely that by using composite materials and a mechanical design that is optimized for this type of structure, the mass at the distal end of the leg can be reduced even further. At the same time, considerable amounts of energy can be stored in the elastic elements. This makes this type of leg particularly suited for energy efficient locomotion that is based on lightweight elastic legs, as shown in the simulations of [26], [27], [28], [29], [30].

References

[1] G. A. Pratt and M. M. Williamson, "Series elastic actuators," in *Proceedings 1995 IEEE/RSJ International Conference on Intelligent Robots and Systems. Human Robot Interaction and Cooperative Robots*, vol. 1, pp. 399–406, IEEE, 1995.

[2] G. A. Pratt, P. Willisson, C. Bolton, and A. Hofman, "Late motor processing in low-impedance robots: Impedance control of series-elastic actuators," in *Proceedings of the 2004 American control conference*, vol. 4, pp. 3245–3251, IEEE, 2004.

[3] J. E. Pratt and B. T. Krupp, "Series elastic actuators for legged robots," in *Unmanned Ground Vehicle Technology Vi*, vol. 5422, pp. 135–144, International Society for Optics and Photonics, 2004.

[4] M. Hutter, C. D. Remy, and R. Siegwart, "Design of an articulated robotic leg with nonlinear series elastic actuation," in *Mobile Robotics: Solutions and Challenges*, pp. 645–652, World Scientific, 2010.

[5] Y. Yesilevskiy, Z. Gan, and C. David Remy, "Energy-optimal hopping in parallel and series elastic one-dimensional monopeds," *Journal of Mechanisms and Robotics*, vol. 10, no. 3, p. 031008, 2018.

[6] J. Pratt and B. Krupp, "Design of a bipedal walking robot," in *Unmanned systems technology X*, vol. 6962, pp. 480–492, SPIE, 2008.

[7] M. Hutter, *StarlETH & Co.: Design and control of legged robots with compliant actuation*. PhD thesis, ETH Zurich, 2013.

[8] N. A. Radford, P. Strawser, K. Hambuchen, J. S. Mehling, W. K. Verdeyen, A. S. Donnan, J. Holley, J. Sanchez, V. Nguyen, L. Bridgwater, *et al.*, "Valkyrie: Nasa's first bipedal humanoid robot," *Journal of Field Robotics*, vol. 32, no. 3, pp. 397–419, 2015.

[9] M. Hutter, C. Gehring, D. Jud, A. Lauber, C. D. Bellicoso, V. Tsounis, J. Hwangbo, K. Bodie, P. Fankhauser, M. Bloesch, *et al.*, "Anymal-a highly mobile and dynamic quadrupedal robot," in *2016 IEEE/RSJ International Conference on Intelligent Robots and Systems (IROS)*, pp. 38–44, IEEE, 2016.

[10] H. M. Herr and A. M. Grabowski, "Bionic ankle–foot prosthesis normalizes walking gait for persons with leg amputation," *Proceedings of the Royal Society B: Biological Sciences*, vol. 279, no. 1728, pp. 457–464, 2012.

[11] R. C. Browning, J. R. Modica, R. Kram, and A. Goswami, "The effects of adding mass to the legs on the energetics and biomechanics of walking," *Medicine & Science in Sports & Exercise*, vol. 39, no. 3, 2007.
[12] U. Saranli, M. Buehler, and D. E. Koditschek, "Rhex: A simple and highly mobile hexapod robot," *The International Journal of Robotics Research*, vol. 20, no. 7, pp. 616–631, 2001.
[13] P. Arm, R. Zenkl, P. Barton, L. Beglinger, A. Dietsche, L. Ferrazzini, E. Hampp, J. Hinder, D. Schaufelberger, C. Huber, *et al.*, "Spacebok: A dynamic legged robot for space exploration," in *International Conference on Robotics and Automation (ICRA 2019)*, 2019.
[14] R. Niiyama, S. Nishikawa, and Y. Kuniyoshi, "Athlete robot with applied human muscle activation patterns for bipedal running," in *2010 10th IEEE-RAS International Conference on Humanoid Robots*, pp. 498–503, IEEE, 2010.
[15] H. Hencky, *Über die angenäherte Lösung von Stabilitätsproblemen im Raum mittels der elastischen Gelenkkette*. PhD thesis, Verlag nicht ermittelbar, 1921.
[16] E. Turco, "Discrete is it enough? the revival of piola–hencky keynotes to analyze three-dimensional elastica," *Continuum Mechanics and Thermodynamics*, vol. 30, no. 5, pp. 1039–1057, 2018.
[17] C. M. Wang, H. Zhang, N. Challamel, and W. Pan, *Hencky bar-chain/net for structural analysis*. World Scientific, 2020.
[18] E. Barchiesi, J. Harsch, G. Ganzosch, and S. Eugster, "Discrete versus homogenized continuum modeling in finite deformation bias extension test of bi-pantographic fabrics," *Continuum Mechanics and Thermodynamics*, pp. 1–14, 2020.
[19] S. G. Krantz and H. R. Parks, *The implicit function theorem: history, theory, and applications*. Springer Science & Business Media, 2002.
[20] C. L. Dym, *Stability theory and its applications to structural mechanics*. Noordhoff, 1974.
[21] A. Isidori, *Nonlinear control systems*, vol. 3. Springer, 1995.
[22] M. Hutter, C. D. Remy, M. A. Hoepflinger, and R. Siegwart, "Scarleth: Design and control of a planar running robot," in *2011 IEEE/RSJ International Conference on Intelligent Robots and Systems*, pp. 562–567, IEEE, 2011.
[23] M. Hutter, C. D. Remy, M. A. Hoepflinger, and R. Siegwart, "Efficient and versatile locomotion with highly compliant legs," *IEEE/ASME Transactions on Mechatronics*, vol. 18, no. 2, pp. 449–458, 2012.
[24] M. Hutter, C. D. Remy, M. A. Hoepflinger, and R. Siegwart, "High compliant series elastic actuation for the robotic leg scarl eth," in *Field Robotics*, pp. 507–514, World Scientific, 2012.
[25] N. Smit-Anseeuw, R. Gleason, P. Zaytsev, and C. D. Remy, "Ramone: a planar biped for studying the energetics of gait," in *2017 IEEE/RSJ International Conference on Intelligent Robots and Systems (IROS)*, pp. 4090–4095, IEEE, 2017.
[26] W. Xi, Y. Yesilevskiy, and C. D. Remy, "Selecting gaits for economical locomotion of legged robots," *The International Journal of Robotics Research*, vol. 35, no. 9, pp. 1140–1154, 2016.
[27] Y. Yesilevskiy, W. Yang, and C. D. Remy, "Spine morphology and energetics: how principles from nature apply to robotics," *Bioinspiration & biomimetics*, vol. 13, no. 3, p. 036002, 2018.
[28] W. Xi and C. D. Remy, "Optimal gaits and motions for legged robots," in *2014 IEEE/RSJ International Conference on Intelligent Robots and Systems*, pp. 3259–3265, IEEE, 2014.
[29] Z. Gan, Y. Yesilevskiy, P. Zaytsev, and C. D. Remy, "All common bipedal gaits emerge from a single passive model," *Journal of The Royal Society Interface*, vol. 15, no. 146, p. 20180455, 2018.
[30] M. Raff, N. Rosa, and C. D. Remy, "Connecting gaits in energetically conservative legged systems," *IEEE Robotics and Automation Letters*, vol. 7, no. 3, pp. 8407–8414, 2022.